



# **Dynamic Failure Processes Under Confining Stress in AlON, a Transparent Polycrystalline Ceramic**

**by B. Paliwal, K. T. Ramesh, James W. McCauley, and Mingwei Chen**

**ARL-RP-269**

**September 2009**

*A reprint from the Proceedings of the 26th Army Science Conference,  
Orlando, FL, 1–4 December 2008.*

## **NOTICES**

### **Disclaimers**

The findings in this report are not to be construed as an official Department of the Army position unless so designated by other authorized documents.

Citation of manufacturer's or trade names does not constitute an official endorsement or approval of the use thereof.

Destroy this report when it is no longer needed. Do not return it to the originator.

# **Army Research Laboratory**

Aberdeen Proving Ground, MD 21005-5069

---

**ARL-RP-269****September 2009**

---

## **Dynamic Failure Processes Under Confining Stress in AlON, a Transparent Polycrystalline Ceramic**

**B. Paliwal**

**Sandia National Laboratories**

**K. T. Ramesh**

**Johns Hopkins University**

**James W. McCauley**

**Weapons and Materials Research Directorate, ARL**

**Mingwei Chen**

**Johns Hopkins University**

**Tohoku University**

*A reprint from the Proceedings of the 26th Army Science Conference,  
Orlando, FL, 1–4 December 2008.*

REPORT DOCUMENTATION PAGE				Form Approved OMB No. 0704-0188	
Public reporting burden for this collection of information is estimated to average 1 hour per response, including the time for reviewing instructions, searching existing data sources, gathering and maintaining the data needed, and completing and reviewing the collection information. Send comments regarding this burden estimate or any other aspect of this collection of information, including suggestions for reducing the burden, to Department of Defense, Washington Headquarters Services, Directorate for Information Operations and Reports (0704-0188), 1215 Jefferson Davis Highway, Suite 1204, Arlington, VA 22202-4302. Respondents should be aware that notwithstanding any other provision of law, no person shall be subject to any penalty for failing to comply with a collection of information if it does not display a currently valid OMB control number. <b>PLEASE DO NOT RETURN YOUR FORM TO THE ABOVE ADDRESS.</b>					
1. REPORT DATE (DD-MM-YYYY) September 2009		2. REPORT TYPE Reprint		3. DATES COVERED (From - To) January 2006–December 2008	
4. TITLE AND SUBTITLE Dynamic Failure Processes Under Confining Stress in AION, a Transparent Polycrystalline Ceramic				5a. CONTRACT NUMBER	
				5b. GRANT NUMBER	
				5c. PROGRAM ELEMENT NUMBER	
6. AUTHOR(S) B. Paliwal, <sup>*</sup> K. T. Ramesh, <sup>†</sup> James W. McCauley, and Mingwei Chen <sup>‡</sup>				5d. PROJECT NUMBER BH64	
				5e. TASK NUMBER	
				5f. WORK UNIT NUMBER	
7. PERFORMING ORGANIZATION NAME(S) AND ADDRESS(ES) U.S. Army Research Laboratory ATTN: RDRL-WM Aberdeen Proving Ground, MD 21005-5069				8. PERFORMING ORGANIZATION REPORT NUMBER ARL-RP-269	
9. SPONSORING/MONITORING AGENCY NAME(S) AND ADDRESS(ES)				10. SPONSOR/MONITOR'S ACRONYM(S)	
				11. SPONSOR/MONITOR'S REPORT NUMBER(S)	
12. DISTRIBUTION/AVAILABILITY STATEMENT Approved for public release; distribution is unlimited.					
13. SUPPLEMENTARY NOTES A reprint from the <i>Proceedings of the 26th Army Science Conference</i> , Orlando, FL, 1–4 December 2008. <sup>*</sup> Sandia National Laboratories, Albuquerque, NM <sup>†</sup> Johns Hopkins University, Baltimore, MD <sup>‡</sup> Johns Hopkins University, Baltimore, MD, and Tohoku University, Sendai, Japan					
14. ABSTRACT An experimental technique is developed to impose a planar lateral confinement in a prismatic specimen (with rectangular cross-section); the setup enabled a controlled and homogeneous stress state with high lateral compressive stresses. A transparent polycrystalline aluminum oxynitride (AION) specimen was used for the study. The statically pre-compressed specimen was then subjected to axial dynamic compressive loading using a modified compression Kolsky bar setup. Experimental design was performed using 3D computational modeling. Initial exploratory experiments were conducted on AION at average planar confinement of 400 – 410 MPa; the results suggested a higher compressive strength and a non-linear stress evolution in AION due to the confinement. A high-speed camera was used to observe the damage evolution in the specimen during the course of loading. The photographs and stress evolution are suggestive of an additional inelastic deformation mechanism, evolution of which is slower than the typical brittle-cracking type of damage apparent in the unconfined case. The TEM and HREM analysis indicated dislocation plasticity in some fragments; dislocations in the slip bands were characterized to be dissociated <110> dislocations on {111} planes. The width between two partial dislocations was about 15 nm, suggesting low stacking fault energy of AION. Microscopic characterization also reveals that the eventual fragmentation of AION is by cleavage mainly along low-index {111} planes.					
15. SUBJECT TERMS aluminum oxynitride, grain-structure related stress raisers					
16. SECURITY CLASSIFICATION OF:			17. LIMITATION OF ABSTRACT  UU	18. NUMBER OF PAGES  18	19a. NAME OF RESPONSIBLE PERSON James W. McCauley
a. REPORT Unclassified	b. ABSTRACT Unclassified	c. THIS PAGE Unclassified			19b. TELEPHONE NUMBER (Include area code) 410-306-0711

# DYNAMIC FAILURE PROCESSES UNDER CONFINING STRESS IN AION, A TRANSPARENT POLYCRYSTALLINE CERAMIC

*B. Paliwal, Sandia National Laboratories, Albuquerque, NM*

*K.T. Ramesh, Johns Hopkins University, Baltimore MD*

*James W. McCauley, Army Research Laboratory, APG, MD*

*Mingwei Chen, Johns Hopkins University, Baltimore MD and Tohoku University, Sendai, Japan*

## Abstract

An experimental technique is developed to impose a planar lateral confinement in a prismatic specimen (with rectangular cross-section); the setup enabled a controlled and homogeneous stress state with high lateral compressive stresses. A transparent polycrystalline aluminum oxynitride (AION) specimen was used for the study. The statically pre-compressed specimen was then subjected to axial dynamic compressive loading using a modified compression Kolsky bar setup. Experimental design was performed using 3D computational modeling. Initial exploratory experiments were conducted on AION at average planar confinement of 400 – 410 MPa; the results suggested a higher compressive strength and a non-linear stress evolution in AION due to the confinement. A high-speed camera was used to observe the damage evolution in the specimen during the course of loading. The photographs and stress evolution are suggestive of an additional inelastic deformation mechanism, evolution of which is slower than the typical brittle-cracking type of damage apparent in the unconfined case. The TEM and HREM analysis indicated dislocation plasticity in some fragments; dislocations in the slip bands were characterized to be dissociated  $\langle 110 \rangle$  dislocations on  $\{111\}$  planes. The width between two partial dislocations was about 15 nm, suggesting low stacking fault energy of AION. Microscopic characterization also reveals that the eventual fragmentation of AION is by cleavage mainly along low-index  $\{111\}$  planes.

## 1. Introduction

There have been several investigations aimed at demonstrating the effects of confinement on the overall compressive behavior of brittle materials like rocks, ceramics and even ice (see e.g. [1; 2; 3] for experiments under quasi-static loading conditions). It is well established that the mechanical behavior of such materials strongly depends on intrinsic stress-concentration regions like micro-flaws, micro-voids and elasticity-mismatch at the grain boundaries. These regions (sometimes called defects) are believed to transform global compressive stresses in to a population of local tensile zones, leading to the activation of tensile cracks [2; 4]. Upon continued loading, these tensile cracks propagate and coalesce, and thereby cause the material to lose its load-carrying capacity. Increase in the confinement inhibits the nucleation of these cracks and also their propagation, which leads to an increase in the material's load carrying capacity (or the compressive failure stress). This phenomenon has been observed a number of times by means of experiments (e.g. [1; 5]) and recently, in analytical/numerical simulations (e.g. [6; 7]). It has also been reported that if the confinement is high enough to significantly suppress the crack-growth, these nominally brittle materials might yield plastically, perhaps achieving an upper limit of the compressive strength [8].

During ballistic impact events, ceramic components are subjected to a combination of varying degrees of confinement and dynamic loading rates. One of the popular experimental methods used in high strain-rate investigations is the well established modified compression Kolsky bar (MKB) technique which generates a homogeneous high strain-rate compressive loading in the range of  $10^2 - 10^4 \text{ s}^{-1}$  [9]. This technique has also been used to examine the effects of confinement on the failure behavior of ceramics undergoing dynamic compression. For example, Chen and Ravichandran [10] conducted recovery

experiments on pre-compressed AlN specimens using MKB. Post-mortem observations suggested that the specimens developed localized conjugate sets of faults containing high crack density in the presence of lateral confinement of 200 MPa (as opposed to axially oriented micro-cracks in its absence). Recently, such recovery experiments were also conducted on SiC-N specimens (in un-published work by H. Wang & K. T. Ramesh in 2003) using metal sleeves to generate lateral confinement of around 335 MPa. They observed the formation of a localized zone of very high crack density in the presence of confinement. Lankford *et al.* [11] have conducted similar recovery experiments on a confined AD-995 alumina specimen where an autofrettage device was used to pre-compress the cylindrical specimen to a hydrostatic pressure of  $\sim 600 \text{ MPa}$ ; the post-mortem results suggested that the confinement caused a failure mode transition from brittle fracture (in the absence of confinement) to extensive multi-slip plastic flow without any macro-cracking in the material. More recently, plate impact recovery experiments conducted on AD-995 alumina [12] suggested a deformation mode transition when the impact pressures were increased from below to above the Hugoniot elastic limit or HEL (from an inter-granular fracture below the HEL to trans-granular cleavage along deformation twins above the HEL).

Thus, the experimental observations suggest that confinement has a profound effect on the overall compressive failure mechanism in ceramics. However, such characterizations have been solely based on post-mortem analysis of the specimen rather than through direct observations of failure processes during the course of loading. Several computational models (e.g. [13; 14; 15]) that attempt to simulate the behavior of brittle materials under complex loading conditions require more fundamental information about failure processes (than can be provided from post-mortem analyses alone).

In this paper, a novel experimental technique is used in conjunction with a high-speed camera to study the *in situ* dynamic failure behavior of materials under confinement. A homogeneous planar confinement is generated in a prismatic specimen along one of the three specimen axes, the dynamic loading is imposed (using MKB) along the second specimen axis and the third axis is used for the ultra-high-speed photography. The confinement level stays relatively uniform, both spatially and temporally, during the course of loading (as determined through numerical simulations). The technique is applied to study the dynamic compressive failure behavior of a transparent polycrystalline aluminum oxynitride (AlON) ceramic under confinement. The unconfined dynamic uniaxial compressive behavior of AlON is presented in our earlier work [16]; hence the present study also aims at providing a comparative analysis of the deformation behavior of AlON with and without the confinement.

In the next section the experimental setup that provides the detailed description of the confining design is discussed, together with a finite element (FE) analysis that simulates the change in the level of constraint during the course of dynamic loading. This is followed by a section on experimental results and discussion and finally by a summary.

## 2. Experimental Setup

### 2.1 Material Investigated

Aluminum oxynitride is a nitrogen stabilized spinel phase of alumina and is compositionally centered at around 35.7mol% AlN and 64.3mol% Al<sub>2</sub>O<sub>3</sub> (equivalent to the stoichiometric composition Al<sub>23</sub>O<sub>27</sub>N<sub>5</sub>). Comprehensive reviews of AlON and AlN-Al<sub>2</sub>O<sub>3</sub> systems can be found in [17; 18]. The mechanical properties of AlON are generally comparable to those of  $\alpha$ -Al<sub>2</sub>O<sub>3</sub>. Owing to its optically isotropic cubic crystal structure, fully dense, polycrystalline bodies can be rendered completely transparent, making it a viable candidate for applications requiring high strength and broad electromagnetic transparency [18; 19]. The material investigated here was fabricated using a proprietary powder processing technique by Surmet Corporation (Burlington, MA) and was obtained in the form of rectangular plates. It was then machined into prismatic specimens 5.2 mm long, with a rectangular cross-section of 4.2 X 2.3 mm. The surfaces were ground and polished within 1  $\mu$ m; the opposite faces were polished parallel to an accuracy of 5  $\mu$ m. Density was determined, using the Archimedes method, to be 3.673 g/cm<sup>3</sup>. Table 1 illustrates the representative properties of polycrystalline AlON (unless otherwise stated, most properties are from Table 2 of Ref. [18]).

### 2.2 Confined Dynamic Compression Experiments

The design of the confinement fixture is shown in Fig. 1. The AlON prismatic specimen (shown in green in the figure) is placed between two very hard steel “T-blocks” made from  $\sim$  HRC 55 hardened AISI 4140 steel alloy. The blocks were polished to obtain precise dimensions and a mirror surface finish. Compressive stress was generated by tightening four high-strength screws that go through four

guide holes and four threaded holes in the top and bottom blocks, respectively.

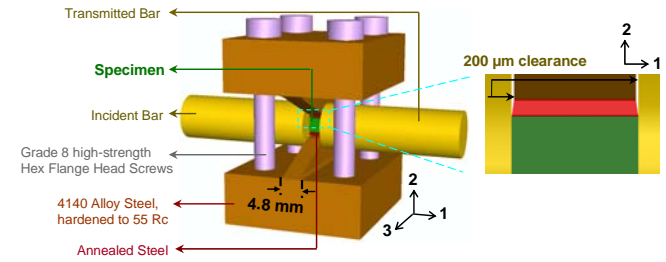


**FIG. 1:** Schematic of the assembly showing the specimen (in green) placed between the two bars (along axis-1) and is constrained in a confining frame that generates lateral stresses along axis-2. The inset shows the chamfered cushion geometry and the clearance between the bars and the T-blocks.

**Table 1**

Property	AlON
Density, g-cm <sup>-3</sup>	3.673 [16]
Hardness, GPa	13.8±0.3 (HK <sub>2</sub> ), 15.5 (HV <sub>2</sub> ) [20]
Young's modulus, GPa	307 – 320
Poisson's ratio	0.25
Compressive strength, GPa	2.22±0.3 at 10 <sup>-5</sup> MPa/μs 3.5±0.25 at 200 MPa/μs [16]
Fracture toughness, MPa-m <sup>1/2</sup>	2.4-2.9, 2.4±0.11[20], 3.96 [21]
Grain size, μm	150 - 200 [22]
Longitudinal speed, kms <sup>-1</sup>	10.13 - 10.3
Shear wave speed, kms <sup>-1</sup>	5.78 - 5.9
HEL, Gpa	10.04 ± 0.7 [23] 11.2 - 12.1 [24] 11 - 11.4 [25] 10.3 - 10.6 [26]

In order to reduce stress concentrations at the specimen-block interfaces and generate a more homogeneous compressive stress state in the specimen, a 500  $\mu$ m thick, soft-annealed AISI 4140 steel ‘cushion’ is sandwiched between the specimen and the T-blocks. Numerical simulations performed using the commercial ABAQUS FE package showed that this appreciably reduces the stress concentrations in the specimen. The inset in Fig. 1 shows the assembly and the geometry of the cushion used in more detail, along with the T-block – specimen and the cushion – specimen interfaces. One of the dimensions of the T-blocks is smaller than the specimen length in order to provide sufficient clearance during the loading (that is, when the assembly is placed between the incident and the transmitted bars, the stresses are transmitted through the specimen alone and the bars do not touch the T-blocks). The cushion has chamfered ends (see the inset in Fig. 1) and covers the entire specimen's surface across its 5.21 mm length.

A torque-wrench is used to control the torque and to ensure that equal torques were applied to all four screws; the torque applied to the bolts is calibrated against the compressive force that is transmitted through the specimen using a cuboid calibration test-sample made from Ti-6Al-4V. A fairly linear relationship between the two is obtained, and this is useful to determine the level of constraint in the specimen *prior* to the high strain-rate compression experiments. In the confined dynamic experiments described here, an average initial confining

stress  $S_{22}$  of 400 – 410 MPa was generated. This confinement level is likely to change during the dynamic loading. A real time measurement of the confining stress during the experiment is difficult to obtain given the sizes and tolerances required in the assembly. Hence, 3D finite element simulations were performed using ABAQUS / STANDARD and EXPLICIT to determine the level of the confinement in the specimen *during* the experiments. The ceramic specimen was modeled using a continuum concrete-damage-plasticity constitutive model and the T-blocks and cushions were modeled using a classical elastic-plastic constitutive model (the simulation details are provided elsewhere [27]). The numerical results show very uniform spatial confinement levels, which increase during the dynamic loading from the initial average value of 400 MPa to an average of ~500 MPa before the unloading begins in the specimen.

Various mechanical confinement techniques have been used in the past, such as a pressure vessel with hydraulic fluid [28] or shrink-fitting a sleeve [29] or an autofrettage device [30]). Our current design is simple to implement, although it does not produce a hydrostatic state. Moreover, it allows *in situ* observation of the failure process, and it generates and maintains relatively uniform confining stresses that either increase or remain relatively constant during the dynamic axial loading.

Fig.2 shows the front view of the assembly (captured by the high-speed camera along specimen axis-3) prior to the dynamic loading. The confining assembly is built in stages, and all of the specimen surfaces are lubricated. The specimen was compressed vertically along axis-2. The entire assembly process was performed on an optical table with a fixture that could hold the bottom T-block while the torque was being applied and maintaining the specimen's position during the entire process. The assembly was then placed between two hard WC platens along the incident and the transmitted bar ends.

The high strain rate compression tests were performed using the well-established Kolsky bar (also called the split-Hopkinson pressure bar); a high-speed camera was also used to observe *in situ* the damage evolution in the specimen. Details related to the Kolsky bar setup and high-speed camera configurations, and complete description of the design is provided in [27]; details pertaining to the diagnostics are provided in [16].

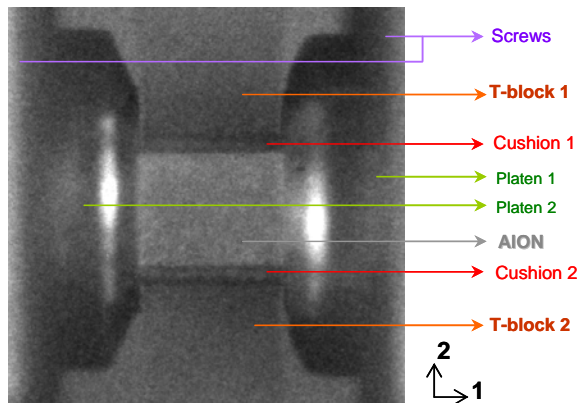


**FIG. 2:** Photograph of the assembly taken from the high-speed camera (along axis-3) showing its individual components prior to the dynamic loading.

### 3. Results and Discussions

The results from the dynamic confined-compression tests are presented as a series of high-speed photographs together with the corresponding axial stress history, indicating the times at which each photographic exposure is made. Fig. 3(a) shows a sequence of frames and a stress-time curve for a confined experiment and, for comparison, Fig. 3(b) shows a single sequence of frames and three stress-time curves from typical unconfined (uniaxial compression) experiments [16]. The numbered points on the stress histories correspond to the times at which the eight numbered photographs were taken (with inter-frame times of 2  $\mu$ s and exposure times of 200 ns for the confined case, and 1  $\mu$ s and 100 ns respectively for the uniaxial case).

Examination of the stress-time curves shown in Fig. 3(a) and 3(b) leads to two specific observations. First, the peak stress of 4.4 GPa in the confined case is substantially greater than that typically attained in unconfined uniaxial compression. Second, the evolution of the axial stress with time is very different in the confined case. There is a pronounced decrease in the rate of change of the axial stress after a stress level of about 3 GPa has been reached (the straight lines in Figure 3 (a) are drawn to demonstrate this). Further, there is a significant time (~3  $\mu$ s) over which the axial stress remains approximately constant near the peak stress before the final stress collapse begins. The unconfined uniaxial compression experiments do not exhibit these features. Thus the examination of the stress-time evolution alone suggests that the macroscopic response to the material is affected by the confinement.

Direct visual evidence of the qualitative difference between the confined and unconfined behaviors can be seen when the high speed photographs of Fig. 3 (a) (the confined case) are contrasted with the photographs in Fig. 3 (b) (the unconfined case). In examining all of these photographs, it should be remembered that the camera and flash illuminators are both on the same side of the specimen, so that newly opened cracks show up as white areas because the crack faces reflect the flash light into the camera sensor. Note first that the appropriate comparison to make is between the last four frames (5-8) in Fig. 3 (a) and the first four frames (1-4) in Fig. 3 (b), since these represent times just before the peak strength is attained in both cases. However, frames (5-8) in Fig. 3 (a) represent 8 $\mu$ s while frames (1-4) in Fig. 3 (b) represent only 4 $\mu$ s. In the unconfined case, clearly defined cracks initiate and grow within the specimen (frames 2 and 3, 3 (b)) and then coalesce to form a well-defined crack cloud (frame 4 of Fig. 3 (b)) at a time close to the peak stress (this is fairly typical in the unconfined case – more observations are presented in [16]). In contrast, frames 5-8 in Fig. 3 (a) for the confined case show no clearly defined cracks, no high-contrast bright regions, and no crack cloud at the time of the peak stress (frame 8 of Fig. 3 (a)). All that is observed is a somewhat misty region, with poorly defined boundaries, that begins close to a platen-specimen interface and then grows slowly in a diffused manner as the stress increases (the frames in Fig. 3 (a) are two  $\mu$ s



apart, while those in Fig. 3 (b) are  $1\ \mu\text{s}$  apart). At the time of the peak stress in the confined sample, there is no evidence of cracking. Frame 8 in Fig. 3 (a) is associated with the peak-stress state in the specimen, but the specimen's appearance does not seem to be dramatically different from that at the commencement of the loading (in contrast to frames 1-4 in Fig. 3 (b)). The diffuse misty regions observed in the confined case do not seem to be indicative of typical 'brittle-cracking' features such as sharp contrast and prominent edges observed in the unconfined case. These visual observations indicate that an additional quasi-elastic deformation mechanism is activated in the confined case before the specimen moves towards a collapse of the stress and final failure. Indeed, in another confined experiment both the high-contrast brittle cracking behavior and the diffuse misty regions were observed, identifying these as two distinct processes.

- Hence, the experimental observations suggest that the confinement not only changes the load carrying capacity of the material, but also affects its overall macroscopic response (which is evident from the axial stress evolution curves). The photographs are suggestive of an additional inelastic (plasticity-like) deformation mechanism, perhaps due to dislocation-induced intra-crystalline slip. The damage evolution due to this inelastic deformation mechanism is demonstrably slower than that due to brittle cracking. Understanding the observed mechanical behavior of AION, as with all ceramics, requires an understanding of the nature of the microstructural features inherent in the material that influence the behavior and that have a variety of antecedent (e.g. some of these features arise from the processing route). As stated in the introduction, a number of these microstructural features result in local stress concentrations, and we call these "defects" for the purposes of this discussion. Examples of such defects include inclusions, pores, secondary phases at grain boundaries, elasticity mismatch at grain boundaries and triple-points, pre-existing microcracks, grain-size inhomogeneities (subsequently referred as Class 1 defects), and even sub-grain features such as twins and stacking faults (referred as Class 2 defects). Each of these types of "defects" is likely to play a different role in the effective mechanical response of the ceramic under different loading conditions. Within a micromechanical framework, Class I defects are generally modeled as elliptical or spherical pores and planar cracks with cohesive and frictional resistance [31; 32]. Under macroscopic uniaxial compression, such defects result in stress concentrations (both mode-I tension and shear) that trigger micro-crack nucleation and subsequent growth. However, the presence of lateral confinement will reduce the stress concentration and suppress micro-crack nucleation, and *also* reduce the driving force for the growth of the microcracks. Thus the action of Class I defects is significantly suppressed by confinement. In contrast, the higher stresses that are developed in the confined case (given the suppression of the role of Class I defects) can result in the growth of Class II defect populations (i.e., twinning, dislocations, stacking faults) and the resulting effective plasticity. Late in the experimental process in these experiments, and particularly once unloading begins, the Class II defects may act as failure-initiation sites as well

(the micro-mechanism sometimes called micro-plasticity induced micro-cracking).

The quantitative character of the "defect" populations in AION is not known. However, a good deal can be inferred about these populations on the basis of specific experimental data. For example, shock compression experiments conducted on alumina specimens have indicated a trend of decreasing HEL with increase in the grain-size and porosity and decrease in the purity [33; 34], and the compressive strength of ceramics has been reported (both through experiments [8] and models [35]) to be a strong function of grain size and Class I defects [15]. Even though the grain-size of AION is an order magnitude greater than that of AD-995, the quasi-static uniaxial compressive strength of AION is comparable to that of AD-995 and the HEL of AION is reported to be higher than that of AD-995 (eg. [36]). This suggests that AION has a comparatively homogeneous microstructure with fewer Class I defects. Recent electron microscopy and chemical analysis [37] have suggested

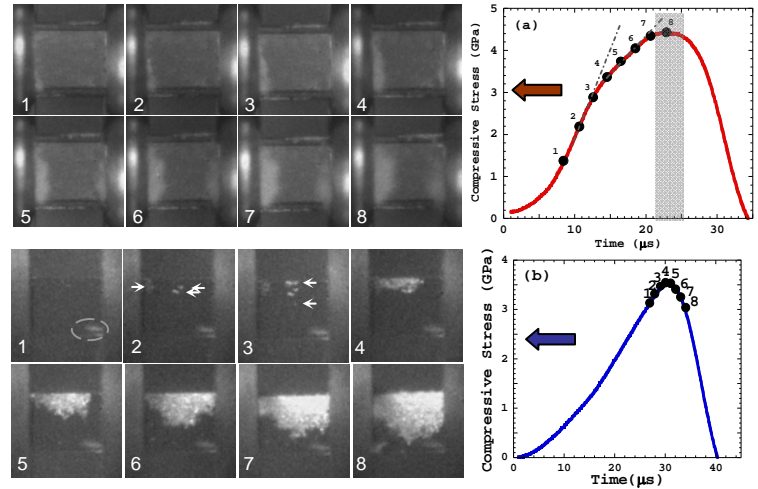


**FIG. 3:** Photographs from the high-speed camera of the dynamic failure process in (a) confined and (b) unconfined AION along with the respective stress evolution curves on the right. The interframe and the exposure time for the confined case are  $2\ \mu\text{s}$  and  $200\ \text{ns}$ , respectively and for unconfined case are  $1\ \mu\text{s}$  and  $100\ \text{ns}$ , respectively (circled region in Frame-1 (and similar for other frames) in 3 (b) shows the flow of the lubricant). Note the damage evolution for the confined case is slower and the region exhibits lower contrast in the photos compared with that of unconfined case; stress evolution curve also suggest a non-linear material response (accompanied by a higher peak stress) which is not evident for the unconfined case.

that this AION has clean grain boundaries that are generally free from glassy phases. In comparison AD-995 is reported to have an aluminosilicate glassy phase [36] with micron and sub-micron sized voids and inclusions that were identified from the grain boundaries and triple junction points [12]. Further, because of the cubic crystal structure of AION, it exhibits better symmetry at the grain boundaries, with smaller stress concentrations due to grain-to-grain elasticity mismatch (as compared to  $\text{Al}_2\text{O}_3$  [38], which has a rhombohedral crystal structure). Table below lists several measurements of the single crystal elastic constants ( $c_{ij}$  using the Voigt notation) of AION



Structure	Isotropic [39]	Isotropic <sup>1</sup>	Isotropic	Isotropic <sup>2</sup>	Cubic <sup>†††</sup>
Method	ultrasound	RUS*	RUS	RUS	RUS
c <sub>11</sub> (GPa)	369.24	391	387	393	392.7
c <sub>44</sub> (GPa)	122.66	129	128	130.9	130.8
c <sub>12</sub> (GPa)	123.92**	132	132	131.2	130.8

\* Resonant Ultrasound Spectroscopy; \*\*  $c_{12} = c_{11} - 2c_{44}$

Thus, it appears that the Class I defect population in this AION is relatively small (at least in comparison to ceramics such as AD995), and we should expect the Class II defects to have a substantial role in the confined experiments.

Under confined conditions, micro-cracking and plasticity are the two major (often competing) sources of the overall apparent inelastic response. Experimental observations have suggested that under uniaxial compression (quasi-static or dynamic), the characteristic of the dominant failure mechanism is that micro-cracks nucleate at various “defects” in the material, and then propagate and interact (see [2; 16]) causing the material to fail. Within the context of *compressive brittle fracture processes*, the effects of the applied strain-rate, inherent flaw distributions and the confinement-levels are paramount and these are addressed below.

- **Strain-rate:** Experimental, numerical and analytical-modeling results [7; 15; 40] have indicated that brittle materials displays a transition to a stronger rate sensitive behavior at a *transition strain-rate* (TSR) beyond which their compressive strength  $\sigma_c$  increases dramatically with the applied rate of loading (strain-rate beyond the TSR are referred as the dynamic strain-rate). This phenomenon is attributed to inertia-dominated dynamic damage evolution in the material in which the rate of micro-crack growth (nucleated from the pre-existing defects in the material) decreases with the increase in the strain-rate, particularly at very-high-rates beyond the TSR. Recent predictions from an interacting micro-crack damage model [15] (in which the inertial effects in the constitutive response arise as a result of crack-growth dynamics) suggests that beyond the TSR, higher strain-rate reduces the stress intensity factor  $K_I$  at the crack tips and thereby inhibits its growth. This also causes the damage-distribution to spread more uniformly over the pre-existing flaw population. Also, results from experiments conducted on various ceramics [41; 42] have indicated a higher fracture toughness value under dynamic loading which further results in higher stresses required to sustain the micro-crack growth as compared to the quasi-static loading. Such crack growth suppression is likely to favor localized plastic flow in the material (causing some slip within the grains) and both micro-plasticity and micro-cracking may contribute to the failure process at the very high rates [43].

- **Defect distributions:** Recent findings from a damage model in which pre-existing flaws are modeled as

closed rectilinear slits (frictional sliding of which causes tensile ‘winged’ cracks to nucleate at their tips under global compression [15]) illustrate the effects of flaw-size distributions on the induced damage and on the compressive strength of the material. This work shows that not only does  $\sigma_c$  increase as the mean flaw-size decreases, but  $\sigma_c$  also increases with the decrease in the spread of the distribution (or the standard deviation with respect to the mean). The model also predicts that materials with lower flaw density  $\eta$  exhibit higher  $\sigma_c$  and display (inertia-dominated) stronger strain-rate sensitivity accompanied by a lower *transition strain-rate*. Recent experimental observations on hot-pressed B<sub>4</sub>C, hot-pressed SiC-N and sintered  $\alpha$ -SiC [40] also supports this result. Similarly, experimental results suggest that under uniaxial compression AION (which has a lower flaw density) exhibits stronger rate-sensitive behavior than AD-995 (for example, a 15% increase in strength with strain rate occurred at  $\sim 58$  MPa/us loading-rate for AION compared to  $\sim 360$  MPa/us for AD-995 alumina<sup>3</sup>). Because the transition to the high rate sensitivity occurs at lower strain-rate in a material with lower flaw density, the effects associated with the decrease in the flaw density are analogous to the dynamic effects associated with the dynamic strain-rate loading [15].

- **Confinement effects:** Lateral confinement inhibits micro-crack nucleation and growth [2], although brittle failure is still dominant if the confinement level is low enough that the stresses do not exceed the critical resolved shear stress (CRSS) required for plastic flow on the crystallographic slip-planes. Crack growth will become significantly more difficult with the increase in the confinement [32] coupled with the increase in strain-rate loading beyond the TSR. As such, it becomes increasingly likely that some slip will result within the grains. It is known that the compressive strength scales approximately linearly with the confining pressure even under a prevailing brittle fracture mode, exhibiting behavior similar to the Drucker-Prager or Mohr-Coulomb failure criterion [44]. Thus even the effects associated with the micro-crack growth can lead to apparent ductility in the constitutive response under large confinement. However, such realizations of the compressive strength are accompanied by localized damage regions in the material with very high crack density, as has been demonstrated both by means of experiments [44] and numerical simulations [7; 45]. Note that such localized damage regions were NOT observed within these confined AION experiments, suggesting that the apparent plasticity that is observed is not due to microcrack growth.

<sup>1</sup> Personal communication to J. W. McCauley by G. Lamberton, University of Mississippi and T. Hartnett, Surmet Corporation

<sup>2</sup> Personal communication to J. W. McCauley by M. Radovic and E. Lara-Curzio, Oak Ridge National Laboratory

<sup>3</sup> Data for AD-995 was obtained from [26]. Compressive strength vs. strain-rate data was converted to compressive strength vs. stress-rate by multiplying the strain-rate by the Young’s modulus. AION data is presented in Fig. 8. The stress-rate at  $\sigma/\sigma_c = 1.15$  is obtained by fitting a power-law function through the available experimental data and then interpolating.

These considerations show that in a material with lower flaw density and subjected to higher confinement and higher strain-rate loading, micro-crack nucleation and growth is suppressed to a higher degree which, therefore, makes it more prone to deform plastically, and that the mode of the visualized deformations is consistent with such an expectation. The mechanisms associated with ceramic behavior when micro-cracking is essentially prohibited either due to very high confinement or very high strain-rates (or both) are of interest. As the confinement and/or the strain-rate loading increases, micro-crack nucleation can be inhibited to such an extent that the stresses in the material can build up sufficiently to allow substantial plastic deformation (e.g.[1]); under such conditions a brittle-to-ductile transition may be realized and nominally brittle material may display a 'limiting strength.' Such conditions might be realized, for example, during indentation-hardness experiments on ceramics (as illustrated in indentation experiments on  $\text{Al}_2\text{O}_3$  [46]) or under tribological loading conditions. During indentation, the region beneath the indenter is effectively confined due to the surrounding medium, and it subsequently yields creating a residual impression on the material surface once the indenter is withdrawn. The equivalent quasi-static yield strength ( $Y_S$ ) can be estimated through the following relation in terms of Vickers hardness ( $H$ )  $Y_S = H/C$ , where  $C$  is a constant, typically  $\sim 3$  for ductile metals (the exact value depending to some extent on the indenter geometry [47]). However, this formulation methodology assumes the material being indented to be rigid-perfectly plastic (with classic von Mises isotropic plasticity) and thus ignores the elastic deformation [48]. Indentation hardness in ceramics can be a strong function of load and often may involve both cracking and plasticity at the loads at which load-insensitive data is typically obtained. Eqn. above thus provides a very approximate measure of strength. An expression for the dynamic equivalent compressive strength can be obtained from the results of plate-impact shock experiments. In such experiments, owing to the uniaxial strain nature of the deformation, the material experiences a very high lateral confinement, and the material also undergoes a very high rate of deformation (where the inertial effects may be sufficient to halt the micro-crack nucleation); this leads to a plasticity dominated behavior. The dynamic equivalent strength  $Y_D$ , obtained in terms of the Hugoniot elastic limit (HEL) based on either the Tresca (or Von Mises) flow criterion is typically expressed as  $Y_D = \text{HEL}(1-2\nu)/(1-\nu)$  [49]. Assuming that the limiting strength follows the equation, and using the values of HEL as 11 GPa and Poisson's ratio of 0.25 for AION, a dynamic equivalent strength of 7.1 GPa is obtained. Assuming the Vickers hardness of AION is 15.5 GPa together with  $C = 3$ , a quasi-static limiting strength can be obtained to be around 5.2 GPa. The degree of approximation of these estimates of limiting strength depends on how much the underlying hypotheses are correct; for instance Eqn. (2) assumes that below the HEL, the material undergoes elastic deformation with no damage initiation. There has been visual evidence of extensive macroscopic cracks in ceramics even when loading is below the HEL (e.g. extensive macro-cracks were seen in the

recovered shock-loaded intact AD 995 alumina specimen when it was shocked to 4 GPa, a stress well below its [12]), but these post-mortem observations may be colored by the unloading process. Recognizing these approximates, these estimates of compressive strength presented in Fig. 4 in the form of a plot of material strength (the equivalent stress) as a function of the loading rate (rather than the strain-rate which is less accurately known in these high strain-rate experiments [50]). Within the same space, results from the uniaxial compression experiments (along with the fitted curve) and confined compression experiments are also plotted. The results from confined compression experiments as well as the earlier uniaxial compression experiments on AION are also presented in the Figure.

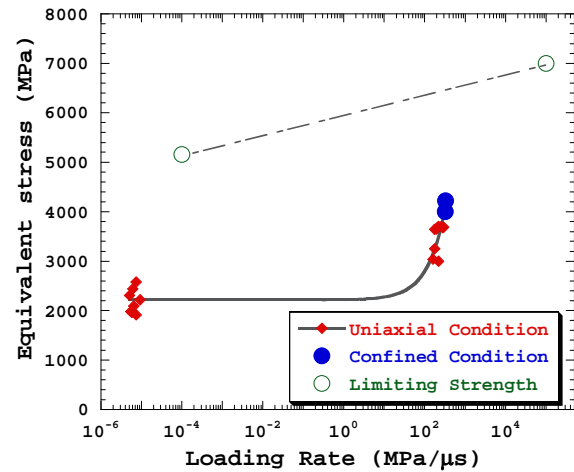


**FIG. 4:** Plot shows the variation of equivalent stress with the loading rate under uniaxial condition (data is plotted as solid diamond and is fitted with a power-law function), confined condition (solid circles) and 'limiting strength' condition realized when full plastic flow is triggered in the material without any micro-cracking (open circles).

Note that the macroscopic equivalent stresses realized during the confined experiments (4.2 GPa) are lower than the limiting equivalent strengths at those loading rates ( $\sim 6.3$  GPa, estimated by interpolating between  $Y_S$  and  $Y_D$ ) needed for plasticity-dominated deformations. However, note also that a stress concentration of only 1.4 – 1.6 is required (e.g. at the triple points) to raise the local stress to the level of the 'limiting strength' and thereby initiate the plastic deformation, e.g. intra-crystalline slip within the grains. Under similar loading conditions Lankford *et al.* [11] reported that the stress evolution curve of the AD-995 alumina specimen confined within the autofrettaged device, was different from the ones obtained under the unconfined condition and showed an apparent plasticity. Postmortem microscopic analysis on the AD-995specimen suggested the activation of multiple slip systems and extensive grain boundary dislocation pile-ups with no apparent macro-cracking. Such plasticity dominated behavior was ascribed to the absence of micro-cracking, aided by the high hydrostatic confinement in the specimen, as the equivalent stresses rose to  $Y_D$ . Moreover, similar dislocation activities and micro-shear dislocation

bands were also observed in the fragments of JS-I<sup>4</sup> alumina tested under unconfined dynamic loading condition in a Kolsky bar; based on such experimental data including microscopic analysis, it was reported that it is possible to reach the plastic limit even under unconfined compression experiments in ceramics which are initially sufficiently flaw free [11]. Similarly, with a polycrystalline ceramic like AlON with “clean” grain-boundaries and relatively few defects (note the transparency) subjected to moderate confinement and high strain-rate loading, it is quite likely that some of the grains might experience limiting stresses and yield plastically. However, if the confinement and the loading rates are not high enough to significantly suppress micro-cracking during the entire loading history, brittle fracture may still be dominant.

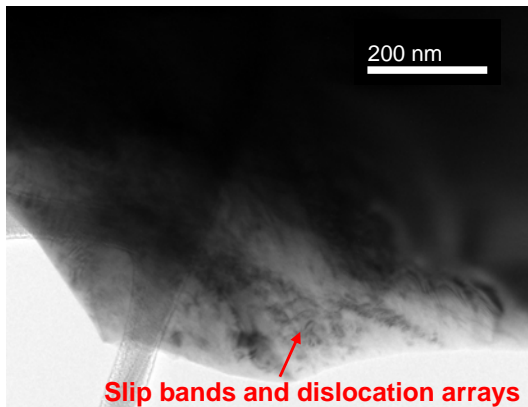


**FIG. 5:** Bright field TEM images of the localized slip-bands composed of dislocation arrays due to plastic deformation in an AlON fragment, after the dynamic confined-compression test.

Therefore, aforementioned numerical and experimental results significantly suggest that the present technique does impose and maintains lateral constraint which results in a significant change in the overall macroscopic response (which is evident from the axial stress evolution curves and the high-speed photographs) and the load carrying capacity of AlON. The damage evolution is demonstrably slower than that due to brittle cracking. We also note that due to the limited spatial resolution of the high-speed camera photographs, it is difficult to deduce the precise nature of the inelastic deformation more clearly for the confined case; however, the comparative analysis on the deformation and the damage evolution between the confined and unconfined cases does indicate the possibility of an additional inelastic deformation in the presence of confinement. Microscopic examinations of the residual debris<sup>5</sup> have indicated dislocation plasticity in some fragments. Fig 5 shows the bright field TEM images of the localized slip bands composed of dislocation arrays in a fragment. These dislocations have not been seen in the as-sintered samples. High-resolution electron microscope (HREM) image (Fig 6) shows that the dislocations in the

slip bands are dissociated into two partial dislocations along  $\langle 110 \rangle$  directions on  $\{111\}$  slip-planes.

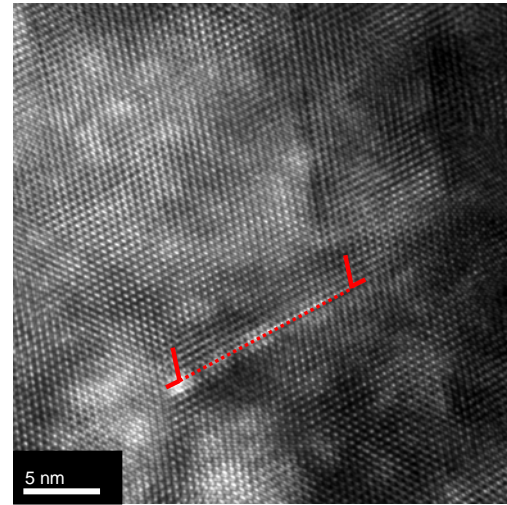


**FIG. 6:** HREM image shows that the dislocations in the slip-bands (see Fig. 5) are dissociated dislocations composed of two partials along  $\langle 110 \rangle$  directions on  $\{111\}$  slip- planes. The width between the two partial dislocations is  $\sim 15$  nm, suggesting low stacking fault energy of AlON.

The dissociation width between the two partials is of about 15 nm, suggesting the low stacking fault energy of AlON. Microscopic characterization of the fragments from both confined and unconfined samples also reveals that the eventual fragmentation of AlON is by cleavage that results in sharp facets of fragments (Fig. 7). However, it is not known at this time if the micro-cleavage characteristics are altered by the confinement. HREM micrographs of the facet edges of the fragments obtained after the dynamic confined-compression tests suggest that the cleavage is mainly along low-index  $\{111\}$  planes.

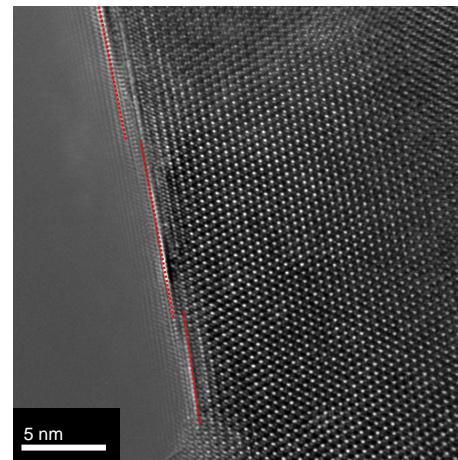


**FIG. 7:** HREM image shows the facet edges of an AlON fragment, obtained after the dynamic confined-compression test; result also suggests that the cleavage facets are parallel to  $\{111\}$  planes with atomic-scale steps.

<sup>4</sup> High purity hot-pressed 99.9 %  $\text{Al}_2\text{O}_3$  with extremely clean and pore free grain boundaries

<sup>5</sup> the final failure process may well involve massive cracking, fragmentation and reloading within the experimental apparatus.

#### 4. Summary

An experimental technique is developed to impose controlled planar lateral-confinement on a specimen subjected to the axial dynamic compressive loading achieved through modified compression Kolsky bar technique. In principle, planar confinement levels as high as 1 GPa can be achieved in the specimen with the help of this technique. The lateral-confinement was implemented by bolting two stiff steel blocks on the lateral surfaces of a prismatic specimen (with a rectangular cross-section). Annealed steel is used as a cushion which is sandwiched between the specimen and the T-blocks to reduce the stress concentrations at the interfaces. FE analysis, conducted to monitor the change in the confinement level during the course of dynamic axial loading, indicates that the confinement level is quite uniform, both spatially and temporally.

The technique was used in conjunction with the high-speed photography to study the dynamic compressive behavior of a transparent polycrystalline AION ceramic under confinement. The high-speed photographs were used to obtain real-time data on the damage kinetics during the compressive failure of AION. Experimental observations suggested that in the presence of lateral confinement – (a) axial stress evolves in a non-linear fashion; (b) there is an apparent increase in the load carrying capacity of the material – as compared with the uniaxial compression experiments with no confinement [16]. High-speed photographs for the confined case suggest an inelastic deformation, evolution of which is slower than the typical brittle-cracking type of damage apparent from the high-speed photographs for the unconfined case shown in [16]. The TEM and HREM analysis on the fragments after these tests indicated dislocation plasticity in some fragments; dislocations in the slip bands were characterized to be dissociated  $\langle 110 \rangle$  dislocations on  $\{111\}$  planes. The width between two partial dislocations was about 15 nm, suggesting low stacking fault energy of AION. Microscopic characterization also reveals that the eventual fragmentation of AION is by cleavage mainly along low-index  $\{111\}$  planes.

## Acknowledgements

This work was performed under the auspices of the Center for Advanced Metallic and Ceramic Systems (CAMCS) at the Johns Hopkins University, supported by the Army Research Laboratory under the ARMAC-RTP Cooperative Agreement No. W911NF-06-2-0006.

## REFERENCE:

- [1] Heard, H. C., and Cline, C. F. (1980): *J. Mater. Sci.* **15**, 1889-1897.
- [2] Ashby, M. F., and Sammis, C. G. (1990): *PAGEOPH* **133**, 489-521.
- [3] Schulson, E. M., Kuehn, G. A., Jones, D. A., and Fifolt, D. A. (1991): *Acta metall. mater.* **39**, 2651-2655.
- [4] Tapponnier, P., and Brace, W. F. (1976): *Int. J. Rock Mech. Min. Sci.* **13**, 103-112.
- [5] Brace, W. F., Paulding Jr., B. W., and Scholz, C. (1966): *J. Geophys. Res.* **71**, 3939-3953.
- [6] Huang, C., and Subhash, G. (2003): *J. Mech. Phys. Solids* **51**, 1089-1106.
- [7] Warner, D. H., and Molinari, J. F. (2006): *Acta mater.* **54**, 5135-5145.
- [8] Rice, R. W. (1971): *Mater. Sci. Res.* **5**, 195-227.
- [9] Ravichandran, G., and Subhash, G. (1994): *J. Amer. Ceram. Soc.* **77**, 263-267.
- [10] Chen, W., and Ravichandran, G. (1996): *J. Amer. Ceram. Soc.* **79**, 579-584.
- [11] Lankford, J., Predebon, W. W., Staehler, J. M., Subhash, G., Pletka, B. J., and Anderson, C. E. (1998): *Mech. Mater.* **29**, 205-218.
- [12] Chen, M. W., McCauley, J. W., Dandekar, D. P., and Bourne, N. K. (2006): *Nature Materials* **5**, 614-618.
- [13] Johnson, G. R., and Holmquist, T. J. (1994): An improved computational constitutive model for brittle materials, pp. 981-984. In S. C. Schmidt, J. W. Shaner, G. A. Samara, and M. Ross (Eds): *High Pressure Science and Technology 1993*, American Institute of Physics, New York.
- [14] Grove, D. J., and Rajendran, A. M. (1994): Modeling of Kipp-Grady plate impact experiments on ceramics using the Rajendran-Grove ceramic model, pp. 749-752. In S. C. Schmidt, J. W. Shaner, G. A. Samara, and M. Ross (Eds): *High Pressure Science and Technology 1993*, American Institute of Physics, New York.
- [15] Paliwal, B., and Ramesh, K. T. (2008): *J. Mech. Phys. Solids* **56**, 896-923.
- [16] Paliwal, B., Ramesh, K. T., and McCauley, J. W. (2006): *J. Amer. Ceram. Soc.* **89**, 2128-2133.
- [17] Corbin, N. D. (1989): *J. Eur. Ceram. Soc.* **5**, 143-154.
- [18] McCauley, J. W. (2001): *Encyclopedia of Materials: Science and Technology*, 127-132.
- [19] McCauley, J. W., and Corbin, N. D. (1979): *J. Amer. Ceram. Soc.* **62**, 476-479.
- [20] Patel, P. J., Swab, J. J., Staley, M., and Quinn, G. D. (2006): *Army Research Laboratory Report - ARL-TR-3852*.
- [21] Xidong, W., Fuming, W., and Wenchao, L. (2003): *Mater. Sci. Engng A* **342**, 245-250.
- [22] Swab, J. J., Gilde, G. A., Patel, P. J., Wereszczak, A. A., McCauley, J. W., and Risner (2001): Fracture Analysis of Transparent Armor Ceramics: *Ceramic Transactions: American Ceramic Society*.
- [23] Thornhill, T. F., Vogler, T. J., Reinhart, W. D., and Chhabildas, L. C. (2005): *Shock Compression of Condensed Matter*, 143-146.
- [24] Sekine, T., Li, X., Kobayashi, T., and Yamashita, Y. (2003): *J. Appl. Phys.* **94**, 4803-4806.
- [25] Cazamias, J. U., Fiske, P. S., and Bless, S. J. (2001): *Shock Compression of Condensed Matter*, 767-770.
- [26] Cazamias, J. U., Bless, S. J., Simha, C. H. M., and Hartnett, T. M. (1999): *Shock Compression of Condensed Matter*, 611-614.
- [27] Paliwal, B., Ramesh, K. T., McCauley, J. W., and Chen, M. (2008): *Amer. Ceram. Soc.* **in press**.
- [28] Anderson Jr., C. E., O'Donoghue, P. E., Lankford, J., and Walker, J. D. (1992): *Int. J. Fract.* **55**, 193-208.
- [29] Chen, W., and Ravichandran, G. (1997): *J. Mech. Phys. Solids* **45**, 1303-1328.
- [30] Lankford, J., Anderson Jr., C. E., Nagy, A. J., Walker, J. D., Nicholls, A. E., and Page, R. A. (1998): *J. Mater. Sci.* **33**, 1619-1625.
- [31] Sammis, C. G., and Ashby, M. F. (1986): *Acta. metall.* **34**, 511-526.
- [32] Horii, H., and Nemat-Nasser, S. (1985): *J. Geophys. Res.* **90**, 3105-3125.
- [33] Bourne, N. K., Rosenberg, Z., Crouch, I. G., and Field, J. E. (1994): *Proc. R. Soc. Lond. A* **446**, 309-318.
- [34] Bourne, N. K. (2001): *Proc. R. Soc. Lond. A* **457**, 2189-2205.
- [35] Bhattacharya, K., Ortiz, M., and Ravichandran, G. (1998): *J. Mech. Phys. Solids* **46**, 2171-2181.
- [36] Dandekar, D. P., McCauley, J. W., Green, W., Bourne, N. K., and Chen, M. (2006): *Proceedings of the 25th Army Science Conference, Orlando FL (to be published)*.
- [37] Chen, M. W., and McCauley, J. W. **Personal Communication**.
- [38] Feng, R. (2007): Microplasticity in Polycrystalline Ceramics under Uniaxial Strain Compression. In K. T. Ramesh (Ed.).
- [39] Graham, E. K., Munly, W. C., McCauley, J. W., and Corbin, N. D. (1988): *Amer. Ceram. Soc.* **71**, 807-812.
- [40] Paliwal, B., and Ramesh, K. T. (2007): *Scripta mater.* **57**, 481-484.
- [41] Weerasooriya, T., Moy, P., and Casem, D. (2006): *J. Amer. Ceram. Soc.* **89**, 990-995.
- [42] Suresh, S., Nakamura, T., Yeshurun, Y., Yang, K.-H., and Duffy, J. (1990): *J. Amer. Ceram. Soc.* **73**, 2457-2466.
- [43] Lankford, J. (1996): *J. Mater. Sci. Letts* **15**, 745-750.
- [44] Chen, W., and Ravichandran, G. (2000): *Int. J. Fract.* **101**, 141-159.
- [45] Nittur, P. G., Maiti, S., and Geubelle, P. H. (2007): *J. Mech. Phys. Solids* **in press**.
- [46] Hockey, B. J. (1971): *J. Amer. Ceram. Soc.* **54**, 223-231.
- [47] Hill, R. (1950): *The Mathematical Theory of Plasticity*. Oxford: Clarendon Press.
- [48] Lankford, J. (1991): *J. Hard Mater.* **2**, 55-77.
- [49] Rosenberg, Z. (1993): *J. Appl. Phys.* **74**, 752-753.
- [50] Jiao, T., Li, Y., and Ramesh, K. T. (2004): *Applied Ceramic Technology* **1**.

NO. OF  
COPIES ORGANIZATION

1 DEFENSE TECHNICAL  
(PDF INFORMATION CTR  
only) DTIC OCA  
8725 JOHN J KINGMAN RD  
STE 0944  
FORT BELVOIR VA 22060-6218

1 DIRECTOR  
US ARMY RESEARCH LAB  
IMNE ALC HRR  
2800 POWDER MILL RD  
ADELPHI MD 20783-1197

1 DIRECTOR  
US ARMY RESEARCH LAB  
RDRL CIM L  
2800 POWDER MILL RD  
ADELPHI MD 20783-1197

1 DIRECTOR  
US ARMY RESEARCH LAB  
RDRL CIM P  
2800 POWDER MILL RD  
ADELPHI MD 20783-1197

ABERDEEN PROVING GROUND

1 DIR USARL  
RDRL CIM G (BLDG 4600)

NO. OF  
COPIES ORGANIZATION

1 ODUSD (SANDT) WS  
L SLOTER  
ROSSLYN PLAZA N  
STE 9030  
1777 N KENT ST  
ARLINGTON VA 22209-2210

1 COMMANDER  
US ARMY MATERIEL CMD  
AMXMI INT  
9301 CHAPEK RD  
FT BELVOIR VA 22060-5527

1 PEO GCS  
SFAE GCS BCT/MS 325  
M RYZYI  
6501 ELEVEN MILE RD  
WARREN MI 48397-5000

1 ABRAMS TESTING  
SFAE GCSS W AB QT  
J MORAN  
6501 ELEVEN MILE RD  
WARREN MI 48397-5000

1 COMMANDER  
WATERVLIET ARSENAL  
SMCWV QAE Q  
B VANINA  
BLDG 44  
WATERVLIET NY 12189-4050

2 COMMANDER  
US ARMY AMCOM  
AVIATION APPLIED TECH DIR  
J SCHUCK  
FT EUSTIS VA 23604-5577

1 NAVAL SURFACE WARFARE CTR  
DAHLGREN DIV CODE G06  
DAHLGREN VA 22448

1 USA SBCCOM PM SOLDIER SPT  
AMSSB PM RSS A  
J CONNORS  
KANSAS ST  
NATICK MA 01760-5057

1 BOB SKAGGS CONSULTANT  
S R SKAGGS  
7 CAMINO DE LOS GARDUNOS  
SANTA FE NM 87501

NO. OF  
COPIES ORGANIZATION

3 AIR FORCE ARMAMENT LAB  
AFATL DLJW  
W COOK  
D BELK  
J FOSTER  
EGLIN AFB FL 32542

1 DPTY ASSIST SCY FOR R&T  
(CD SARD TT  
Only) ASA (ACT)  
J PARMENTOLA  
THE PENTAGON RM 3E479  
WASHINGTON DC 20310-0103

1 US ARMY ARDEC  
AMSTA AR AE WW  
E BAKER  
BLDG 3022  
PICATINNY ARSENAL NJ  
07806-5000

11 US ARMY TARDEC  
AMSTRA TR R MS 263  
K BISHNOI  
D TEMPLETON (10 CPS)  
WARREN MI 48397-5000

1 COMMANDER  
US ARMY RSRCH OFC  
A RAJENDRAN  
PO BOX 12211  
RSRCH TRIANGLE PARK NC  
27709-2211

2 CALTECH  
G RAVICHANDRAN  
T AHRENS MS 252 21  
1201 E CALIFORNIA BLVD  
PASADENA CA 91125

5 SOUTHWEST RSRCH INST  
C ANDERSON  
K DANNEMANN  
T HOLMQUIST  
G JOHNSON  
J WALKER  
PO DRAWER 28510  
SAN ANTONIO TX 78284

2 UNIV OF DELAWARE  
DEPT OF MECH ENGR  
J GILLESPIE  
NEWARK DE 19716

NO. OF  
COPIES ORGANIZATION

3 SRI INTERNATIONAL  
D CURRAN  
D SHOCKEY  
R KLOOP  
333 RAVENSWOOD AVE  
MENLO PARK CA 94025

1 APPLIED RSRCH ASSOCIATES  
D GRADY  
4300 SAN MATEO BLVD NE  
STE A220  
ALBUQUERQUE NM 87110

1 INTERNATIONAL RSRCH  
ASSOCIATES INC  
D ORPHAL  
4450 BLACK AVE  
PLEASANTON CA 94566

2 WASHINGTON ST UNIV  
INST OF SHOCK PHYSICS  
Y GUPTA  
J ASAY  
PULLMAN WA 99164-2814

1 COORS CERAMIC CO  
T RILEY  
600 NINTH ST  
GOLDEN CO 80401

1 UNIV OF DAYTON  
RSRCH INST  
N BRAR  
300 COLLEGE PARK  
MS SPC 1911  
DAYTON OH 45469-0168

2 COMMANDER  
US ARMY TACOM  
AMSTA TR S  
T FURMANIAK  
L PROKURAT FRANKS  
WARREN MI 48397-5000

1 PROJECT MANAGER  
ABRAMS TANK SYSTEM  
J ROWE  
WARREN MI 48397-5000

1 CERCOM  
R PALICKA  
991 PARK CENTER DR  
VISTA CA 92083

NO. OF  
COPIES ORGANIZATION

3 COMMANDER  
US ARMY RSRCH OFC  
B LAMATINA  
D STEPP  
W MULLINS  
PO BOX 12211  
RSRCH TRIANGLE PARK NC  
27709-2211

1 NAVAL SURFACE WARFARE CTR  
CARDEROCK DIVISION  
R PETERSON  
CODE 28  
9500 MACARTHUR BLVD  
WEST BETHESDA MD 20817-5700

4 LAWRENCE LIVERMORE NATL LAB  
R GOGOLEWSKI L290  
R LANDINGHAM L369  
J E REAUGH L282  
S DETERESA  
PO BOX 808  
LIVERMORE CA 94550

4 SANDIA NATL LAB  
J ASAY MS 0548  
L CHHABILDAS MS 0821  
D CRAWFORD ORG 0821  
M KIPP MS 0820  
PO BOX 5800  
ALBUQUERQUE NM 87185-0820

3 RUTGERS  
THE STATE UNIV OF NEW JERSEY  
DEPT OF CRMCS & MATLS ENGRNG  
R HABER  
607 TAYLOR RD  
PISCATAWAY NJ 08854

2 THE UNIVERSITY OF TEXAS  
AT AUSTIN  
S BLESS  
IAT  
3925 W BRAKER LN STE 400  
AUSTIN TX 78759-5316

3 SOUTHWEST RSRCH INST  
C ANDERSON  
J RIEGEL  
J WALKER  
6220 CULEBRA RD  
SAN ANTONIO TX 78238



NO. OF  
COPIES ORGANIZATION

6 GDLS  
W BURKE MZ436 21 24  
G CAMPBELL MZ436 30 44  
D DEBUSSCHER MZ436 20 29  
J ERIDON MZ436 21 24  
W HERMAN MZ435 01 24  
S PENTESCU MZ436 21 24  
38500 MOUND RD  
STERLING HTS MI 48310-3200

1 INTERNATL RSRCH ASSN  
D ORPHAL  
4450 BLACK AVE  
PLEASANTON CA 94566

1 JET PROPULSION LAB  
IMPACT PHYSICS GROUP  
M ADAMS  
4800 OAK GROVE DR  
PASADENA CA 91109-8099

3 OGARA HESS & EISENHARDT  
G ALLEN  
D MALONE  
T RUSSELL  
9113 LE SAINT DR  
FAIRFIELD OH 45014

2 CERADYNE INC  
M NORMANDIA  
3169 REDHILL AVE  
COSTA MESA CA 96626

3 JOHNS HOPKINS UNIV  
DEPT OF MECH ENGRNG  
K T RAMESH  
3400 CHARLES ST  
BALTIMORE MD 21218

2 SIMULA INC  
V HORVATICH  
V KELSEY  
10016 51ST ST  
PHOENIX AZ 85044

3 UNITED DEFENSE LP  
E BRADY  
R JENKINS  
K STRITTMATTER  
PO BOX 15512  
YORK PA 17405-1512

NO. OF  
COPIES ORGANIZATION

10 NATL INST OF STANDARDS & TECH  
CRMCS DIV  
G QUINN  
STOP 852  
GAITHERSBURG MD 20899

2 DIR USARL  
AMSRD ARL D  
C CHABALOWSKI  
V WEISS  
2800 POWDER MILL RD  
ADELPHI MD 20783-1197

ABERDEEN PROVING GROUND

65 DIR USARL  
RDRL WM  
S KARNA  
J MCCAULEY (20 CPS)  
J SMITH  
T WRIGHT  
RDRL WMB  
J NEWILL  
M ZOLTOSKI  
RDRL WMM  
S MCKNIGHT  
R DOWDING  
RDRL WMM C  
R SQUILLACIOTI  
RDRL WMM D  
E CHIN  
K CHO  
G GAZONAS  
J LASALVIA  
P PATEL  
J MONTGOMERY  
J SANDS  
RDRL WMS  
T JONES  
RDRL WMT  
P BAKER  
B BURNS  
RDRL WMT A  
P BARTKOWSKI  
M BURKINS  
W GOOCH  
D HACKBARTH  
T HAVEL  
C HOPPEL  
E HORWATH

NO. OF  
COPIES ORGANIZATION

M KEELE  
D KLEPONIS  
H MEYER  
J RUNYEON  
S SCHOENFELD  
RDRL WMT C  
T BJERKE  
T FARRAND  
K KIMSEY  
L MAGNESS  
S SEGLETES  
D SCHEFFLER  
R SUMMERS  
W WALTERS  
RDRL WMT D  
J CLAYTON  
D DANDEKAR  
M GREENFIELD  
E RAPACKI  
M SCHEIDLER  
T WEERASOORIYA  
RDRL SL  
R COATES

NO. OF  
COPIES ORGANIZATION

3 FRAUNHOFER-INSTITUT FÜR  
KURZZEITDYNAMIK (EMI)  
PROF DR K THOMA  
DIPL-PHYS E STRAßBURGER  
AM KLINGELBERG 1 D – 79588  
EFRINGEN-KIRCHEN  
GERMANY